A Complete Set of Elastic moduli of a molecular spin-crossover solid: spin-state dependence, cooperativity and mechanical actuation

Mirko Mikolasek,[1] Maria D. Manrique-Juarez,[2-3] Helena J. Shepherd,[4] Karl Ridier,[2] Sylvain Rat,[2] Victoria Shalabaeva,[2] Alin-Ciprian Bas,[2] Ines Collings,[1] Aleksandr Chumakov,[1] Thierry Leichle,[3] Liviu Nicu,[3] William Nicolazzi,[2] Gábor Molnár,[2] Lionel Salmon[2] and Azzedine Bousseksou[2,*]

[1]*ESRF-The European Synchrotron, CS40220, 38043 Grenoble Cedex 9 France*
[2]*LCC-CNRS, Université de Toulouse, CNRS, Toulouse, France*
[3]*LAAS-CNRS, Université de Toulouse, CNRS, Toulouse, France*
[4]*School of Physical Sciences, University of Kent, Canterbury, CT2 7NH, UK*

Keywords: elastic properties, spin crossover, crystal structure, cooperativity, actuators

ABSTRACT: Molecular spin crossover complexes are promising candidates for mechanical actuation purposes. The relationships between their crystal structure and mechanical properties remain, however, not well understood. In this study, combining high pressure synchrotron X-ray diffraction and nuclear inelastic scattering measurements, we assessed the effective macroscopic bulk modulus (11.5 ± 2.0 GPa), Young's modulus (10.9 ± 1.0 GPa) and Poisson's ratio (0.34 ± 0.04) of the spin crossover complex $[Fe^{II}(HB(tz)_3)_2]$ (tz = 1,2,4-triazol-1-yl) in its low spin state. Crystal structure analysis revealed a pronounced anisotropy of the lattice compressibility, which was correlated with the difference in spacing between the molecules in different crystallographic directions. Switching the molecules from the low spin to the high spin state leads to a remarkable drop of the Young's modulus to 7.1 ± 0.5 GPa, which was also assessed in thin film samples by means of micromechanical measurements. These results are in agreement with the high cooperativity of the spin crossover in this compound and highlight its application potential in terms of recoverable stress (21 ± 1 MPa) and work density (15 ± 6 mJ/cm^3).

1. Introduction

Spin-crossover (SCO) complexes of certain transition metal ions constitute a prominent example of smart, multifunctional molecular materials that exhibit a reversible change of their molecular spin-state from a low-spin (LS) to a high-spin (HS) electronic configuration under the application of a variety of external stimuli such as temperature or pressure variations, light irradiation, etc.[1-2] This spin-state conversion is accompanied by a drastic change of optical, magnetic, electrical and mechanical properties of the material providing scope for different applications.[3-4]

In the solid state the strong electron-lattice coupling in certain SCO compounds can lead to the emergence of cooperative effects such as first-order phase transitions and associated hysteresis phenomena (bistability). This cooperativity has been extensively investigated since the early stages of SCO research and today it is generally agreed that it can be attributed to a combination of short- and long-range elastic interactions, which arise primarily from the significant volume change of the coordination octahedron upon the SCO (ca. 25 % for $Fe^{II}N_6$)[5]. Spiering *et al.*[6] have proposed a model based on elasticity theory, in which the cooperativity of the thermally induced spin transition is governed by the stiffness of the crystal lattice (*i.e.* the bulk modulus) and the magnitude of the volume mismatch between the HS and LS molecules. The confrontation of this model with experimental data obtained in SCO complexes suggests that the anisotropic character of the elastic parameters as well as the anharmonicity of the lattice should be also fully considered.[7-8] A detailed knowledge of the crystal structure and elastic properties of SCO materials is then essential for rationalizing their cooperativity. It is thus rather surprising that while numerous structural studies have been reported on SCO compounds, their elastic properties remain largely unknown. The few studies performed so far often provided incomplete information and were mainly limited to only one spin state.[9–18]

The need for the accurate determination of the elastic/mechanical properties of SCO materials is not only crucial for the fundamental understanding of the SCO phenomenon, but also for engineering purposes. Indeed, recently it was proposed that the lattice volume change (typically 1–10 % in most SCO materials), that accompanies the spin transition, can be readily exploited for actuating purposes.[19] Various actuating devices, mainly consisting of bilayer structures where a SCO thin film is coated on a freestanding cantilever, have been then constructed and investigated for their actuating properties in response to the spin-state change of the thin film.[19-25] Obviously, the actuating performance of these devices, in particular the actuating force and work density, is directly related to the elastic properties (Young's modulus, Poisson's ratio, …) of the SCO material, which need to be accurately characterized.

The primary goal of the present work is to perform a detailed characterization of the elastic properties of a SCO compound in the two spin states, and to analyze the relationships with the SCO phenomenon both from the fundamental and engineering points of view. For this purpose, we selected the mononuclear SCO complex $[Fe^{II}(HB(tz)_3)_2]$ (tz = 1,2,4-triazol-1-yl) **(1)**, which exhibits an isostructural and abrupt first-order spin transition between its LS (t_{2g}^6) and HS ($t_{2g}^4 e_g^2$) configurations near room temperature (*ca.* 335 K) with a narrow thermal hysteresis loop (*ca.* 1 K) and a remarkable mechanical resilience upon repeated switching.[26] Several studies using optical microscopy methods revealed exceptionally fast switching kinetics in single crystals of **(1)**, demonstrating that thermomechanical properties certainly play a crucial role in the spin transition properties in this molecular compound.[27-28] Moreover, this neutral complex is one of the few evaporable SCO compounds and **(1)** was used to synthesize high-quality thin films by vacuum deposition methods.[29] It turned out that the spin transition properties of the films are close to those encountered in the bulk material, even though well-characterized finite-size effects were observed.[30] Thin films of **(1)** were then integrated into micro-electromechanical systems (MEMS) for actuation purposes.[31] As we will see later, this latter method can be used as an original means to extract the elastic properties of the thin films.

In this paper, we combined micromechanical resonance experiments on MEMS cantilevers with nuclear inelastic scattering (NIS) and high-pressure synchrotron X-ray diffraction (XRD) measurements to obtain a complete picture of the elastic properties of the SCO complex **(1)** in its different forms (single crystal, powder and thin films). The combination of these different experimental techniques allowed the determination of a unique combination of elastic constants, including the bulk modulus, the Poisson's ratio, the Debye sound velocity and the Young's modulus. In addition the spin-state dependence as well as the anisotropic character of these parameters could be also assessed and discussed with respect to the crystal structure, the cooperativity of the SCO and the actuating properties.

2. Results

2.1. Nuclear inelastic scattering

To characterize the elastic properties of the crystalline powder, lattice dynamical parameters have been determined using resonant nuclear inelastic scattering (NIS). This technique is based on the Mössbauer effect and enables the vibrational modes of the iron atoms to be probed.[32-33] NIS spectra were collected in the two spin states at 295 K (LS) and 360 K (HS). The iron vibrational density of states (DOS), shown in **Figure 1**, was extracted from the NIS spectra following the procedure described in ref. [33]. In particular, the use of powdered samples leads

to the determination of an iron-partial DOS averaged over all directions of phonon polarizations (*i.e.* over all directions of atomic displacements).

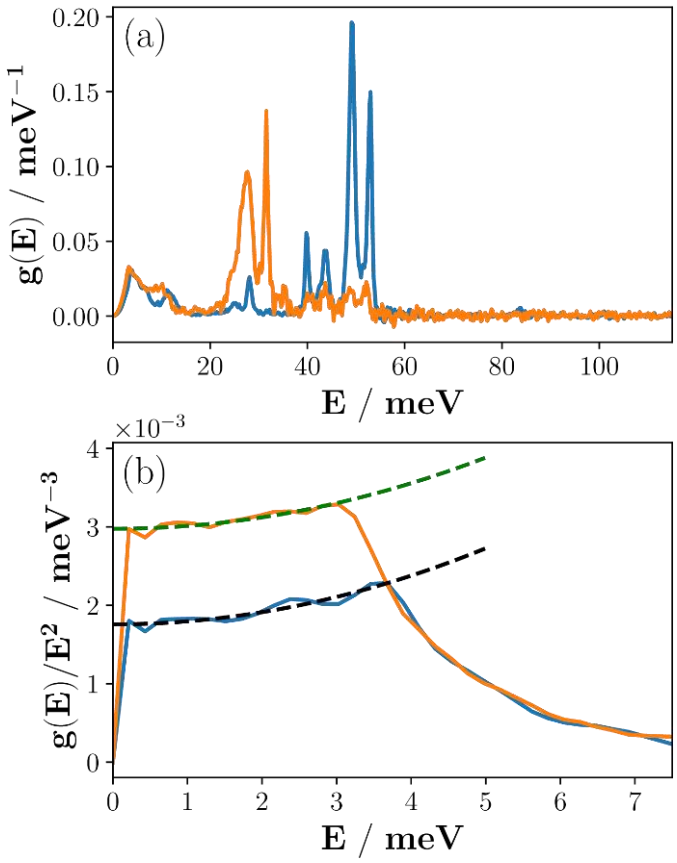

Figure 1. (a) Partial-iron density of vibrational states at 295 K in the LS (blue) and at 360 K in the HS (orange) states. (b) Reduced density of vibrational states (full line) in the LS (blue) and HS (orange) states. The dashed lines are the result of the fits used to extrapolate the experimental data to $E = 0$.

As displayed in **Figure 1a**, an important blueshift of the optical modes is observed when going from the HS to the LS state. This drastic change of the vibrational frequencies associated with the coordination sphere is a well-known feature of the SCO phenomenon. It is the consequence of the electronic reconfiguration of the *d* orbitals of the central metal ion, with a higher occupancy of the antibonding e_g orbitals in the HS state and a subsequent weakening of the metal-ligand bonds.[1] The spin-state change leads to a sizeable modification of the lattice stiffness as well, which can be observed in the low-energy part of the phonon spectra, associated with long-wavelength acoustic modes. From the low-energy limit of the DOS, we can use the Debye model to extract the Debye sound velocity in the two spin states as follows[34-35]:

$$\lim_{E\to 0} g(E) \approx g_D(E) = \frac{m}{2\pi^2 \rho \hbar^3 v_D^3} E^2 \qquad (1)$$

where $g(E)$ and $g_D(E)$ are the experimental and the Debye normalized densities of state, respectively, m is the mass of the resonant nucleus (^{57}Fe), ρ is the density of the material, $\hbar$ is the reduced Planck constant and v_D is the Debye sound velocity. The calculated Debye sound velocities are $v_{D,LS}(T = 295\ \mathrm{K}) = 1810 \pm 45\ \mathrm{m \cdot s^{-1}}$ and $v_{D,HS}(T = 360\ \mathrm{K}) = 1550 \pm 36\ \mathrm{m \cdot s^{-1}}$ in the LS and HS states, respectively. These measurements reveal thus a significant increase of the sound velocity by 17 % upon the HS to LS transition.

In the case of isotropic materials, it is possible to estimate the Young's modulus from the Debye sound velocity. Although this compound exhibits highly anisotropic properties (*vide infra*), this approximation remains valid for the specific case of randomly oriented materials (*e.g.* a powder), which are isotropic macroscopically and can be described therefore by an effective Young's modulus. As reported in ref. [15], the Young's modulus *Y* is related to v_D through the following relationship:

$$\mathrm{Y} = \left(\frac{2\alpha + \beta}{3}\right)^{\frac{2}{3}} \rho \mathrm{v_D^2} \quad (2)$$

with:

$$\alpha = [2(1+\nu)]^{\frac{2}{3}} \quad (3)$$

and

$$\beta = \left[\frac{(1-2\nu)(1+\nu)}{1-\nu}\right]^{\frac{2}{3}} \quad (4)$$

where ν is the Poisson's ratio. At this step, this parameter is unknown and we assume a value of $\nu = 0.3 \pm 0.1$ as it is considered in a large range of materials. This value will be refined in the next part of the article from the XRD results. The calculated effective Young's moduli (obtained for a randomly oriented powder sample) are $Y_{LS} = 10.9 \pm 1.0$ GPa and $Y_{HS} = 7.1 \pm 0.5$ GPa for the LS and HS states, respectively.

2.2. X-ray diffraction under pressure

X-ray diffraction measurements under high pressure were carried out on a single crystal of **(1)** at room temperature (in the LS state). **Figure 2** shows the pressure dependence of the lattice parameters and the unit-cell volume. These measurements were restrained to the LS state but, unlike the NIS experiments, enable the anisotropic character of the structural and elastic properties of **(1)** to be probed.

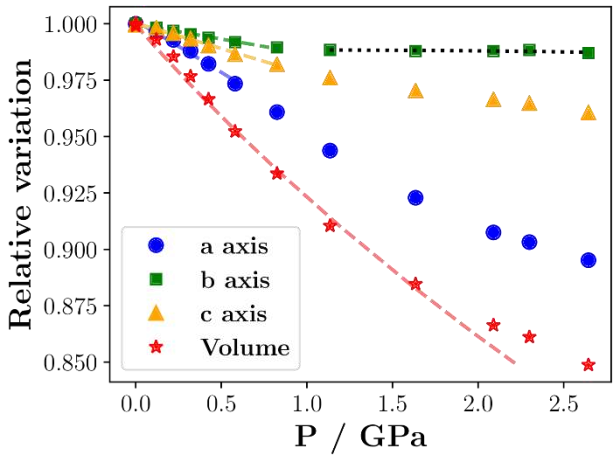

Figure 2. Pressure dependence of the lattice parameters and unit-cell volume derived from single-crystal X-ray diffraction measurements. Dashed lines are the fitted curves used for the extraction of the elastic parameters. The dotted line underlines the incompressibility of the *b*-axis.

The bulk modulus B was extracted by fitting the *P-V* curve using the extensively used second-order Birch-Murnaghan equation of state.[36] We did not take into account the points above 1.7 GPa because of the loss of the hydrostaticity and the solidification of the Daphne oil pressure transmitting medium around 2 GPa. In these conditions, the effective bulk modulus is evaluated at $B = 11.5 \pm 2$ GPa. Considering the previously calculated effective Young's modulus, we can refine the effective Poisson's ratio at $\nu = 0.34 \pm 0.04$ using the expression:

	$3B = Y/(1\text{-}2\nu)$	(5)

This value is consistent with our initial assumption ($\nu = 0.3 \pm 0.1$). It is important to note again that this 'effective value' refers to the macroscopic, randomly oriented material, which was used for the NIS measurements.

Indeed, some interesting properties of this material are mainly due to its pronounced anisotropy, which can be further analyzed from the XRD data. In **Figure 2**, distinct behaviors are clearly evidenced along the three crystallographic directions. For example, it appears that the material becomes uncompressible above *ca.* 0.7 GPa along the *b*-axis. In order to investigate the anisotropic character of the elastic properties of **(1)** in the LS state in a more quantitative way, it is possible to calculate an effective unidirectional bulk modulus through:

	$\epsilon_\gamma = \frac{\Delta\gamma}{\gamma_0} = -\frac{1-\nu_{\gamma\alpha}-\nu_{\gamma\beta}}{Y_\gamma}P = -\frac{1}{3C_\gamma}P$	(6)

where ϵ_γ is the strain along the γ axis due to the pressure P, C_γ is the effective unidirectional bulk modulus along the γ axis ($\alpha, \beta, \gamma, =$ a, b or c and $\alpha \neq \beta \neq \gamma$) and $\nu_{\gamma\alpha}$ are the Poisson's ratio. For small strains, it is worthwhile to note that: $\frac{1}{B} = \frac{1}{3}(\frac{1}{C_a} + \frac{1}{C_b} + \frac{1}{C_c})$. These and other

elastic parameters extracted from NIS and high-pressure X-ray diffraction measurements are summarized in **Table 1**.

Table 1. Elastic parameters of **(1)** derived from NIS and high pressure XRD measurements

Parameter	LS (T = 295 K)	HS (T = 360 K)
$v_D\ (m \cdot s^{-1})$	1810 ± 45	1550 ± 36
$Y\ (GPa)$	10.9 ± 1.0	7.1 ± 0.5
$B\ (GPa)$	11.5 ± 2.0	
ν	0.34 ± 0.04	
$C_a(GPa)$	7.9 ± 1.0	
$C_b(GPa)$	25 ± 2.0	
$C_c(GPa)$	15 ± 2.0	

2.3. Micromechanical analysis

Recently, the integration of SCO materials into MEMS devices for actuating purposes also provided an original way to probe the mechanical properties of thin films[18,25]. These devices basically consist of freestanding silicon micro-cantilevers coated with a thin SCO film. The actuation of the bilayer system at its resonance frequency f_r allows some important information about the mechanical characteristics of the SCO thin film to be extracted. In particular, the resonance frequency shift Δf_r of the cantilever due to the deposition of the SCO material (see **Figure 3**) can be correlated with the elastic modulus (Y_{SCO}) as follows:

$$\Delta f_r = f_{bi} - f_s \quad (7)$$

where f_s and f_{bi} are the resonance frequency before and after the deposition, respectively. They can be calculated using[25, 37]:

$$f_r = \frac{\beta_0^2}{2\pi L^2}\sqrt{\frac{D}{\rho_{Si}A_{Si} + \rho_{SCO}A_{SCO}}} \quad (8)$$

where f_r is the resonance frequency of the structure, $\beta_0 = 1.8751$, $A_i = t_i w_i$ is the cross-section surface of the layer i with t_i and w_i the thicknesses and width. D is expressed by:

$$D = \frac{wt^3 E_1}{12}\frac{mn}{(1+m)^3(1+mn)}\left[3(1+m^2) + (1+mn)\left(m^2 + \frac{1}{mn}\right)\right] \quad (9)$$

where $t = t_{SCO} + t_{Si}$, $m = t_{SCO}/t_{Si}$ and $n = Y_{SCO}/Y_{Si}$.

Eq. 8 can be used only for well-shaped devices, high-quality films and good dimensional control in general. In a previous work we succeeded to integrate molecules of **(1)** into MEMS for actuation purposes.[23] Nevertheless the multilayer structure of the device, required for SCO actuation-detection, limited the accurate determination of the elastic modulus of **(1)**. In order to extract this parameter with a better accuracy, in the present work the

mechanical device was simplified according to the microfabrication protocol described in Ref. [18]. A 210-nm-thick film of **(1)** was deposited by thermal evaporation on monolithic Si microcantilevers following the procedure described in Ref. [29]. Then, the resonance frequency of 15 cantilevers was assessed at room temperature, before and after the SCO film deposition, by means of a home-made optical Fabry-Perot interferometer (**Figure 3**).[38] **Table 2** summarizes the main parameters of these bilayer cantilever systems. The Young's modulus of the spin crossover layer was estimated by fitting the experimental data using **Equation 8**. As a result, a Young's modulus of $Y_{LS} = 12.0 \pm 1.5\ GPa$ is obtained for the thin films of **(1)** in the LS state. A word of caution, however, is necessary as the model does not take into account the anisotropy. Notably, the extracted value is related to the elastic constant of the material along the length of the cantiveler, *i.e.* an averaged value of *a* and *b* crystallographic axes in the case of films of **(1)**, which are oriented with the orthorhombic *c*-axis normal to the substrate. Second, due to the anisotropy, we cannot properly speak about Young's modulus as several other elastic constants from the stiffness tensor may be involved in the extracted value. In the following, we refer to effective Young's modulus instead of Young's modulus.

Table 2. MEMS geometry and elastic properties of thin films of **(1)** extracted from micromechanical experiments

	Silicon	**Thin film of (1)**	
		LS (293 K)	HS (353 K)
Density ρ (kg.m^{-3})	2330 [39]	1568 [27]	1485*
Elastic constant Y (GPa)	169 [39]	**12.0 ± 1.4**	**9.9 ± 1.4**
	Bilayer cantilever		
Modal coefficient λ_1	1.875		
Length L (µm)	50		
Width w (µm)	9.5		
Thickness t_{SCO} (µm)	0.210		
Thickness t_{Si} (µm)	2.471		
f_s (kHz)	1362 ± 9		
f_{bi} (kHz)	1336 ± 9		
Δf_r (kHz)	-25.25 ± 1.4		

*This value takes into account also the mass conservation.

The effective Young's modulus of the films of **(1)** in the HS state cannot be determined experimentally using the same method because of the impossibility of heating the cantilevers above the spin transition temperature with our Fabry-Perot set-up. Nevertheless, this value can be deduced from our previous work[23] using Equation 7, taking into account the previously reported experimental shift of the resonance frequency (and the geometry) of the MEMS associated with the LS to HS transition ($\Delta f_r = -66\ Hz$). Using the effective Young's modulus of the LS state, and assuming a volume change only in the axis orthogonal to the surface

($\Delta t_{SCO}/t_{SCO}$= +5.6 %), we can estimate the effective Young's modulus in the HS state as $Y_{HS} = 9.9 \pm 1.5\ GPa$. It is interesting to compare the values of Y obtained for the films (Y_{LS}/Y_{HS} = 12.0/9.9 GPa) with those obtained for the corresponding powder material (Y_{LS}/Y_{HS} = 10.9/7.1 GPa). We can notice that both the absolute values and the spin-state dependence of the Young's modulus are in reasonably good agreement in the bulk and the film samples close to the error bars of the measurements.

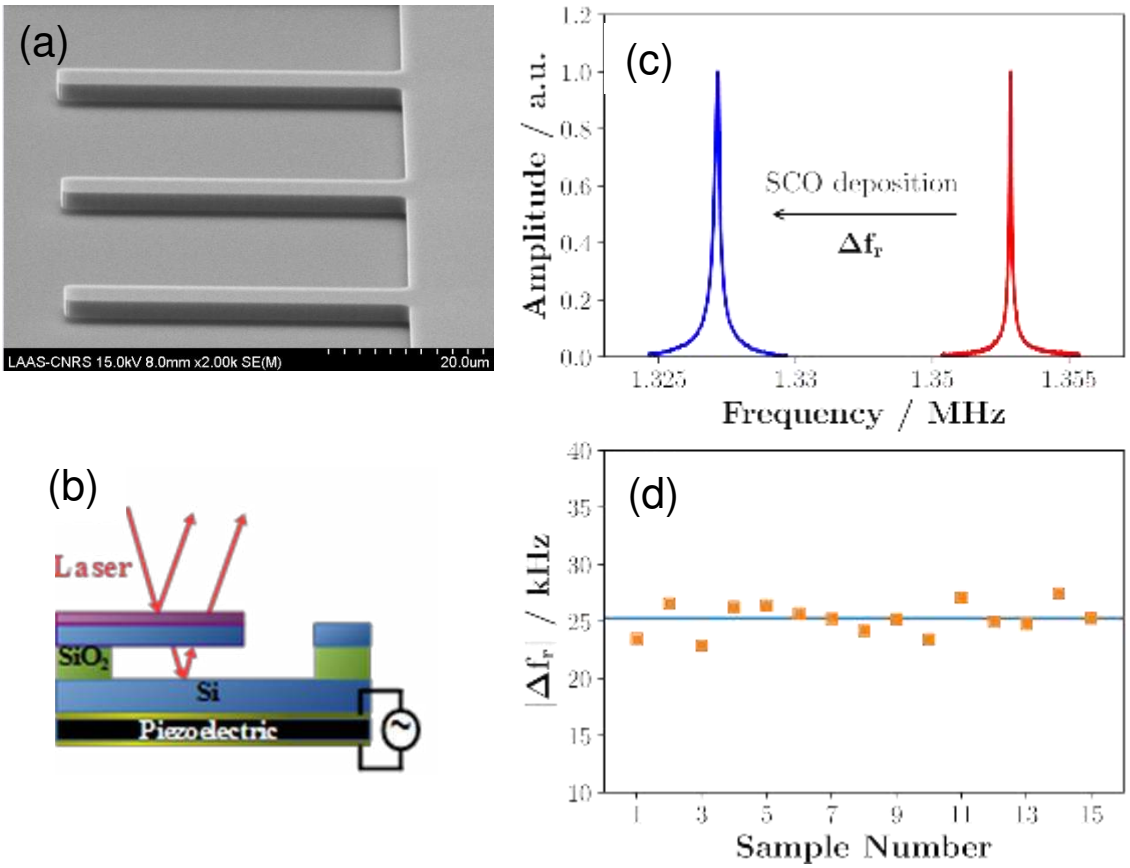

Figure 3. (a) SEM image of the MEMS cantilevers. (b) Scheme of the Fabry-Perot measurement setup. (c) Typical resonance frequency curves measured before and after the deposition of the thin film of **(1)**. (d) Resonance frequency shifts due to SCO film deposition in 15 different devices.

3. Discussion

3.1. Elastic moduli and crystal structure

Table 3 gathers the sparse literature data published on effective (*i.e.* isotropically averaged) elastic moduli of different SCO complexes. It should be noted that the reported error bars are usually of the order of 0.5 - 1 GPa, but in most cases this does not refer to the *accuracy*, but only to the *precision* of the measurements. Indeed, the accuracy of the extracted values are often

reduced by different approximations inherent to the data treatment (choice of models, fitting procedures, etc.) and remains difficult to evaluate.

Table 3. Comparison of reported elastic moduli of different SCO complexes

Compound	Elastic modulus (GPa)	Method	Sample
$Fe(phen)_2(NCS)_2$	B_{HS} = 9.3, B_{LS} = 12.2	XRD[10]	Single crystal
$Fe(btz)_2(NCS)_2$	B_{HS} = 8.3, B_{LS} = 11.2	XRD[10]	Single crystal
$Fe(dpp)_2(NCS)_2$.py	B_{HS} = 10.6	XRD[11]	Single crystal
[{Fe(bpp)$(NCS)_2$}(4,4'-bpy)].2MeOH	B = 6.2*	XRD[12]	Single crystal
[Fe(TPA)(TCC)]SbF6	B_{LS} = 10.8	XRD[13]	Single crystal
[Fe(3-MeOsalEen)$_2$]PF_6	B_{HS} = 4.3	XRD[40]	Single crystal
$[Fe(hptrz)_3](OTs)_2$	Y_{HS} = 1.3, Y_{LS} = 1.7	AFM[14]	Film
$[Fe(ptz)_6](BF_4)_2$	B_{HS} = 4.8	Brillouin spectra[9]	Single crystal
	Y_{HS} = 4.5		
	v_{HS} = 0.34		
[Fe(pyrazine)$(Ni(CN)_4)$]	Y_{HS} = 10.4, Y_{LS} = 13.5	NIS[15]	Crystalline powder
[Fe($H_2B(pz)_2$(phen)]	Y_{HS} = 4.7, Y_{LS} = 5.2	NIS[16]	Crystalline powder
	Y_{HS} = 6.9	MEMS[18]	Amorphous film
{Fe(3-CNpy)$[Au(CN)_2]_2$}·2/3H_2O	Y_{LS} = 7.5	Cantilever bending[19]	Single crystal
$[Fe(HB(tz)_3)_2]$ (from this work)	Y_{HS} = 7.1, Y_{LS} = 10.9	NIS	Crystalline powder
	B_{LS} = 11.5	XRD	Single crystal
	v_{LS} = 0.34		
	Y_{HS} = 9.9, Y_{LS} = 12.0	MEMS	Crystalline film

*Averaged value for the HS and LS states

Overall, both the bulk and the Young's moduli of the investigated SCO compounds fall in the range of *ca.* 4 – 13 GPa despite their very significant structural differences (e.g. ionic or neutral, mono or polynuclear, solvated or not). On the basis of these data we expect therefore that most SCO complexes shall be characterized by comparable elastic moduli. Unfortunately, such small differences of elastic properties are very difficult to trace back to specific structural details due to the large number of parameters involved. A notable exception is the case of $[Fe(hptrz)_3](OTs)_2$ (where hptrz = 4-heptyl-1,2,4-triazole and OTs = tosylate), which is a relatively soft SCO compound – presumably due to the presence of the alkyl chains. Indeed, aliphatic substituents have been successfully used to tune the melting temperature of liquid crystalline SCO complexes[41] and also to alter the SCO properties of iron-triazole complexes.[42] This approach appears thus as a viable strategy to modulate (*i.e.* reduce) their stiffness as well. Unfortunately, the practically more interesting opposite case, i.e. lattice stiffening, seems to be considerably more difficult to achieve by molecular engineering.

In the case of the isotropic approximation, there are only two independent elastic constants. Hence if one can determine both the bulk and the Young's moduli it becomes possible to calculate all other elastic parameters. Of particular interest for engineering purposes is the Poisson's ratio, which has been extracted for **(1)** in the present work and previously for the $[Fe(ptz)_6](BF_4)_2$ (ptz = 1-propyltetrazole) complex by Jung et al.[9] In both cases a value of $\nu = 0.34$ has been obtained, which is a typical value for most common materials. Notably, using a similar methodology, the Poisson's ratio was also evaluated for the truly isotropic (cubic) Prussian blue analogue complex Ni/$[Fe(CN)_6]$ and a value of $\nu = 0.35$ was found.[43] It may be worth to note also that for $\nu = 0.33$ one obtains $B = Y$. In addition, the temperature dependences of the isotropic bulk and Young's moduli are the same, hence the Poisson's ratio is temperature-independent within this approximation. By the same token one may expect that the spin-state dependence of ν will be rather weak as well. (Obviously, if the anisotropy is taken into account this may not be the case at all.)

The present measurements demonstrate also that, as can be expected, significant changes occur in the elastic properties with the spin-state conversion. In particular, the HS → LS transition is characterized by an increase of the Debye sound velocity and the isotropic Young's modulus by 17 % and 50 %, respectively. These spin-state-dependent variations can be compared with only a few other SCO materials (**Table 3**). Overall these data reveal the decrease of the elastic moduli by *ca.* 10-50 % when going from the LS to the HS state. In a simple approach this can be understood by considering the volume dependence of the bulk modulus in the Debye-Grünesisen approximation of the anharmonic lattice[9]:

$$\frac{\Delta B}{B} = -2\gamma\frac{\Delta V}{V} \qquad (10)$$

where γ is the Grüneisen parameter, which typically takes values between 1-3. Taking into account the typical volume change associated with the SCO ($\frac{\Delta V_{SCO}}{V} = 1 - 10\ \%$) the experimentally observed variations of B can be considered reasonable.

Importantly, it appears that the structural and elastic changes accompanying the transition in **(1)** are also strongly anisotropic. This is deduced from the structural data, which show that the changes of the cell parameters along the three crystallographic axes are markedly different and even of opposite sign ($\Delta a/a$ = -2.3 %, $\Delta b/b$ = +1.0 % and $\Delta c/c$ = +5.6 %) during the thermal LS to HS transition.[27] This must result in an anisotropic variation of the elastic modulus (increase along the *a*-axis and decrease along the two other crystallographic directions). Moreover, the X-ray diffraction measurements under pressure show that the mechanical and elastic properties of this compound exhibit a strong anisotropy with, especially, a higher value

of the unidirectional bulk modulus along the *b*-axis (the stiffness along this direction is three times larger than along the *a*-axis), which can be clearly depicted from **Figure 4**. A plausible explanation for this anisotropic contraction is the difference in spacing between the molecules: more space is seen in the *a*-direction, which could explain its higher compressibility. The distance between Fe centers in ambient conditions along the *a*-axis is 13.3332(4) Å, while the equivalent distance along the *b*-axis is 8.7654(2) Å (equal to the unit cell axes as a consequence of the space group symmetry).[27]

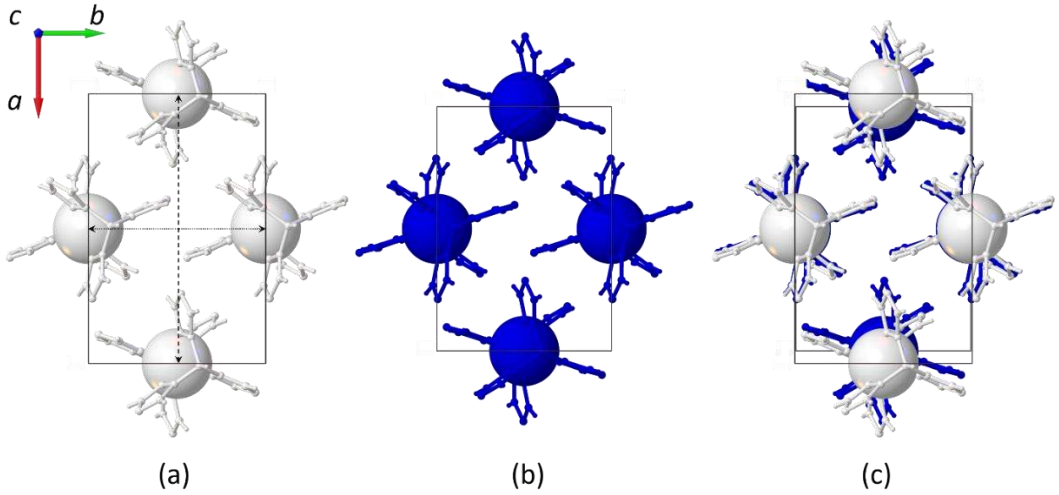

Figure 4. View of a layer of molecules of **(1)** in the *ab* plane at (a) 0.12 GPa and (b) 2.09 GPa. The two are also shown overlaid in (c). Fe atoms are shown as large spheres, all other atoms are depicted using a ball and stick model.

A Hirshfeld surface comparison of the structures at 0.12 GPa and 2.09 GPa was used to further investigate the anisotropic compression in terms of different intermolecular interactions in each direction, as shown in **Figure 5**.

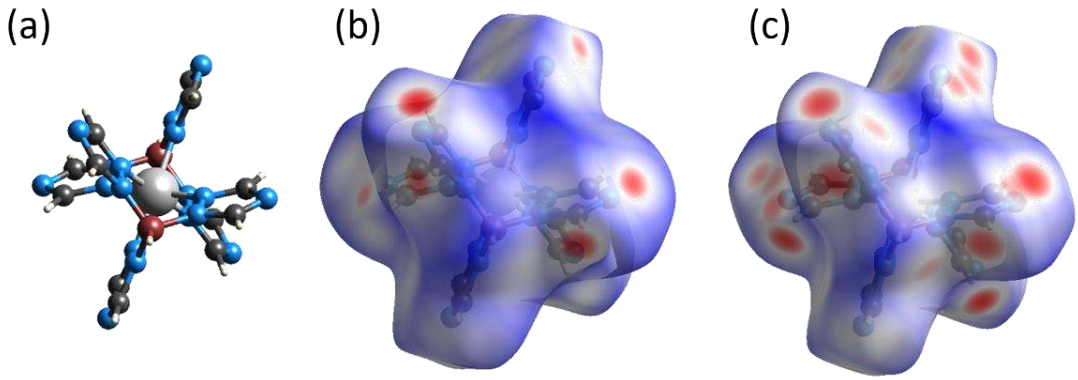

Figure 5. Hirshfeld surface analysis of **(1)** as a function of pressure. (a) shows the molecular structure viewed down the *c*-axis. Hirshfeld surfaces with d_{norm} mapped onto the surface are drawn for the structure at (b) 0.12 GPa and (c) 2.09 GPa. The molecule is centrosymmetric, so the back side is identical.

Details of the technique are described elsewhere,[44] but briefly, a Hirshfeld surface encloses a volume of space around a molecule in which the electron density from the enclosed molecule is greater than that contributed by its neighbors. When mapped with the property d_{norm} it provides a simple visual description of contacts across the whole molecule; red areas represent regions of the molecule interacting with adjacent molecules at less than the sum of the van der Waals radii, while blue indicates distances greater than the sum of the van der Waals radii. As expected, close contacts between molecules increase as the pressure is increased, a result of the reduced void space in the crystal. This is evident from the increased proportion of red areas on the surface at higher pressures. Close inspection of these red regions reveal that they comprise C-H···N and H···H interactions with adjacent molecules. Further insight can be obtained from examining a fingerprint plot of all interactions in the structure at each pressure,[45] as shown in **Figure 6**.

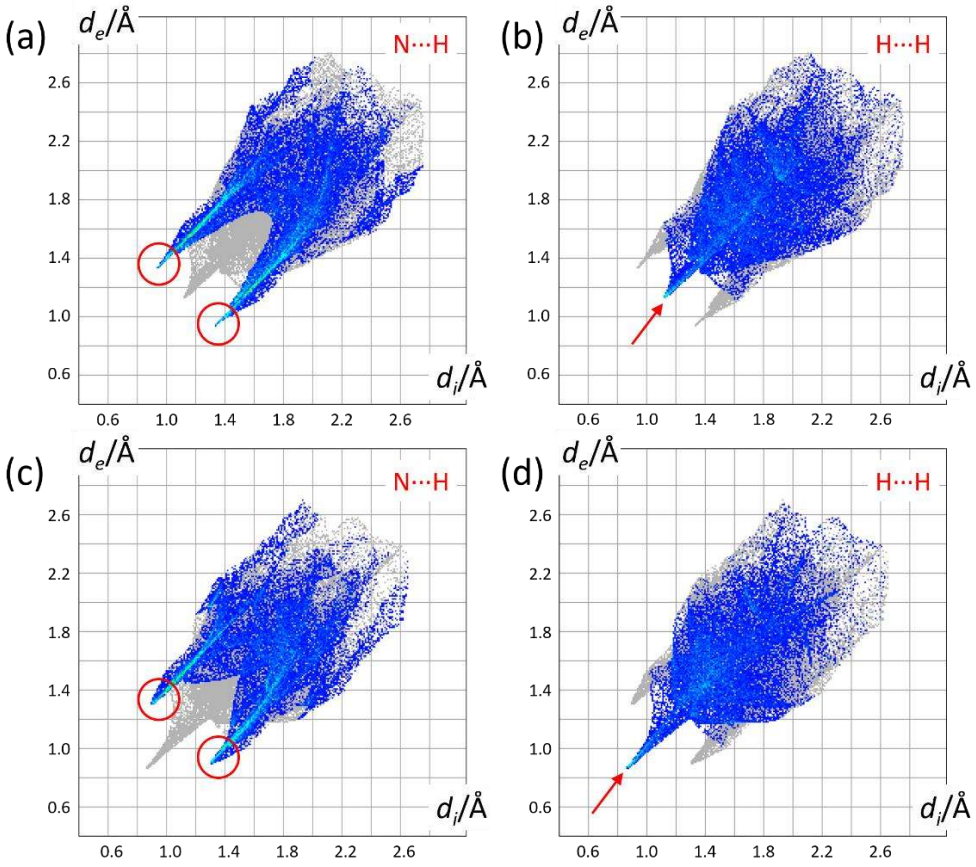

Figure 6. Fingerprint plots showing the distance to the nearest internal (d_i) and external (d_e) atoms for points on the Hirshfeld surface at 0.12 GPa ((a) and (b)) and 2.09 GPa ((c) and (d)). Interactions between N and H atoms are highlighted in (a) and (c) and interactions between H atoms are highlighted in (b) and (d). Red arrows and circles are discussed in the text.

As expected, pressure causes a shift in the fingerprint as a whole towards the origin, a consequence of the increase in density between 0.12 and 2.09 GPa. More interesting is the relative shifts between the different types of interactions at the surface. The shortest C-H···N interactions do not shift significantly on the application of pressure, indicated by red circles in **Figure 6** (a) and (c), and thus reveals these interactions to be relatively stiff. By contrast, the H···H interactions are much softer, reducing in distance significantly in the same pressure range (indicated by red arrows in **Figure 6** (b) and (d)). The final values of less than 1.7 Å represent the effective limit for these types of interactions under pressure, before repulsive interactions dominate.[46] The distribution of the stiffest C-H···N interactions in the *a*- and *b*-directions were further investigated in an effort to determine the anisotropic origin of the compressibility, as shown in **Figure 7**. In **Figure 7a** it is apparent that these stiff interactions form a dense network along the *b*-direction, which cannot be thus compressed without reducing the distance of these. By contrast, these interactions form a zig-zag motif along the *a*-direction, as shown in **Figure 7b**. This motif allows for facile contraction along the *a*-axis simply by changing the angles rather than modifying the distances.

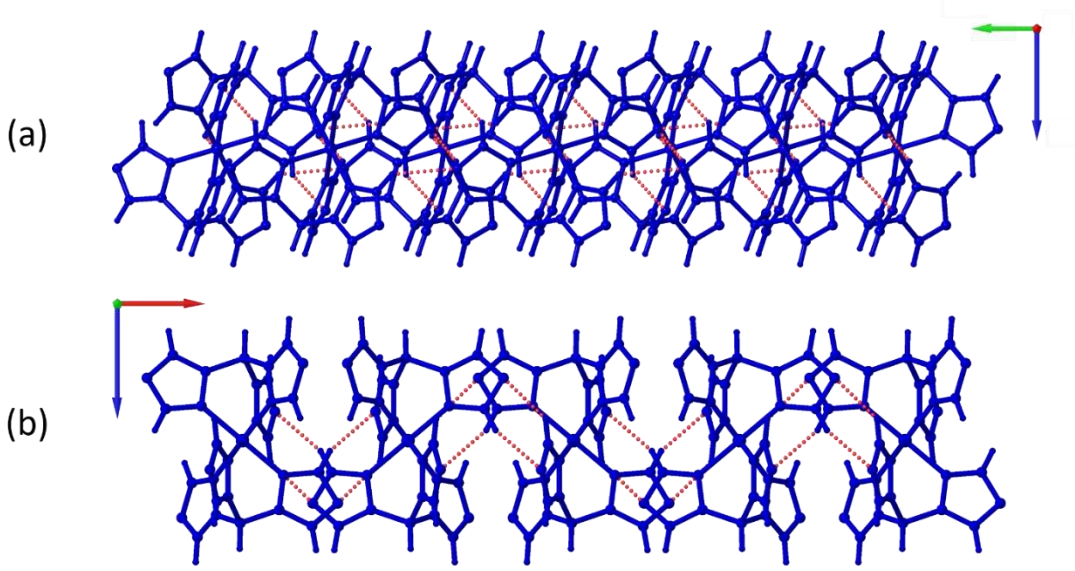

Figure 7. Packing of a sheet of molecules (blue) that propagates infinitely in the *ab*-plane connected by short C-H···N interactions (red dotted lines). Views in the (a) *bc*-plane and (b) *ab*-plane.

3.2. Elastic moduli and the spin transition

In SCO compounds, the lattice compressibility and the volume misfit between the HS and LS molecules represent the two key ingredients to obtain cooperative effects, driven by the elastic interactions between the SCO molecules.[6-8] As mentioned above this rough picture is further complicated by the specific properties of the crystal lattice, such as its anharmonicity,

anisotropy and low-wavelength phonon spectrum. Besides long-range interactions, which arise due to the change of the elastic energies, in certain cases, short-range interactions may also occur due to specific nearest-neighbor couplings leading to a change of the ligand field (and/or vibrational frequencies) of the neighbor molecule(s). These latter phenomena have been evoked in particular for polynuclear SCO systems – mostly on a phenomenological basis.[47-48] From the point of view of structural chemistry, strong cooperativity of the SCO is usually associated with large structural differences between the HS and LS molecules (*i.e.* differences in size and shape) and/or with the crystal packing involving numerous, strong intermolecular contacts (e.g. π-π, hydrogen and van der Waals bonds).[49]

Using the above mentioned lattice dynamical and structural indicators it is interesting to compare compound **(1)** with the fully characterized $Fe^{II}(btz)_2(NCS)_2$ **(2)** (btz = 2,2'-bi-4,5-dihydrothiazine) and [Fe^{II}(pyrazine)$Ni(CN)_4$] **(3)** complexes (**Table 3**). The mononuclear complex **(2)** is the archetype of non-cooperative SCO solids: it exhibits a very gradual spin conversion between *ca.* 170 and 290 K, which is associated with a small interaction parameter Γ = 163 (32) cm^{-1} when analyzed in the frame of the classical Slichter-Drickamer model (**Figure 8**).[50] The HS and LS forms of **(2)** are isostructural and, in the absence of notable strong interactions, the lattice cohesion is achieved by van der Waals interactions.[51] The stiffness (B_{HS} = 8.3 GPa) of the lattice of **(2)** falls in the 'ordinary' range for SCO solids and the same holds for the variation of the unit cell volume upon the SCO ($\Delta V_{SCO}/V$ = 3.8 %).[10] On the other hand, the three-dimensional (3D) coordination network **(3)** is the archetype of highly cooperative SCO solids: it exhibits a very abrupt spin transition around 292 K with a 25 K hysteresis width, which is associated with a large interaction constant Γ = 565 (9) cm^{-1} (**Figure 8**).[52] The HS and LS forms of **(3)** are isostructural and the lattice cohesion is achieved by the strong 3D covalent network wherein the ferrous ions are directly linked by small bridging ligands. As a consequence the lattice stiffness (Y_{HS} = 10.4 GPa) of **(3)** is rather high among SCO solids and the unit cell volume change upon the SCO ($\Delta V_{SCO}/V$ = 15 %) is one of the highest reported values.[53] At a first glance, compounds **(1)** and **(2)** appear very similar in that **(1)** is also a mononuclear complex with an isostructural spin transition whose structure exhibits no appreciable strong intermolecular interactions (despite numerous weak C-H···N contacts). The lattice stiffness (Y_{HS} = 7.1 GPa) and the HS-LS volume change ($\Delta V_{SCO}/V$ = 4.6 %) are also comparable with those reported for **(2)**. Yet, compound **(1)** displays a first-order spin transition at 335 K with a 1 K wide hysteresis, associated with a very large value of the interaction parameter Γ = 483 (6) cm^{-1} (**Figure 8**), which is comparable with compound **(3)**. (*N.B.* The hysteresis width should never be taken as a direct measure of the cooperativity as it depends

not only on the interaction parameter, but also on the reciprocal transition temperature $1/T_{SCO}$.) From the data acquired for **(1)** we suspect that its outstanding behavior in terms of cooperativity is related to the strong anisotropy of the lattice strain upon the SCO, which is known to give rise to additional contributions to the elastic interaction energy.[54] Notably, one can note that the stiffness of the lattice in the *c*-direction is relatively high (C_c = 15 GPa) whereas the strain along this axis is also particularly high ($\Delta c/c$ = +5.6 %), a combination of which possibly represent an important contribution to the cooperativity of the material. It is important to stress, however, that the interaction constant is only of the order of 10^2 cm^{-1}, i.e. several orders of magnitude smaller than (for example) the ligand field energy. In other words, tiny differences of interaction constants arise from the combination of a large number of structural parameters, which remains thus extremely difficult, if not impossible, to rationalize.[54]

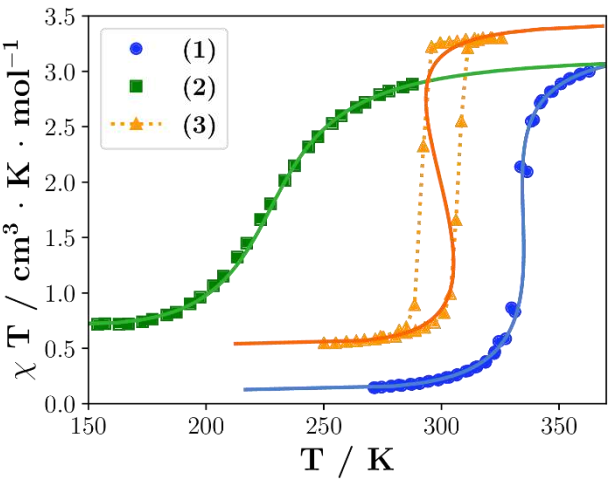

Figure 8. Spin transition curves of compounds **(1)** – **(3)**. The data were replotted from refs. [27], [51] and [53], respectively. The full-lines correspond to the fitted curves using the Slitcher and Drickamer model.

It is important to note also that the anisotropic character in the change of the structural and elastic properties during the spin transition is potentially also an important ingredient to reduce the resistive forces that impede the propagation of the phase boundaries during the nucleation and growth process accompanying the first-order spin transition.[28] These resistive forces come mainly from the structural misfits and the inhomogeneous accommodation strains between the LS and HS phases, and participate in the slowing down of the phase boundary propagation due to the existence of internal elastic frictions and mechanical losses. Thus, anisotropic changes in the elastic/structural properties may allow to better accommodate the volume change and the structural deformations (minimizing the excess elastic energy) throughout the phase transition. This is also an important characteristic that could explain the proven resilience of single crystal

and thin films of **(1)** upon repetitive thermal cycles and then the excellent reproducibility of the spin transition always observed in this compound.

3.3. Elastic moduli and mechanical actuation

Using the experimentally determined Young's modulus and Poisson's ratio we have re-analyzed the data reported in ref. [23] about actuation of silicon MEMS devices by films of **(1)**. In this previous work the static deflection of MEMS cantilevers due to the SCO was tracked by means of an integrated piezoresistive detection. In the present work, using an external optical detection method, introduced recently in ref. [25], we were able to calibrate the piezoresistance changes in terms of deformation amplitude (**Figure 9**) and then calculate the relevant actuating properties of **(1)**. From this calibration of the system, the actuating deflection amplitude Δz due to the spin transition is $476\ nm$. The curvature κ of the cantilever can be deduced as follows[25]:

$$\kappa = -\frac{2\Delta z}{L^2} \quad (11)$$

The curvature is directly related to the strain of the SCO layer ϵ_{SCO} along the cantilever axis by:

$$\epsilon_{SCO} = \frac{t\left[3(1+m^2)+(1+mn)\left(m^2+\frac{1}{mn}\right)\right]}{6(1+m)^2}\kappa \quad (12)$$

A curvature of $\kappa = -23.8\ m^{-1}$ and a strain of $\epsilon_{SCO} = -0.17 \pm 0.05\ \%$ are obtained, where the negative value denotes the contraction of the film along the cantilever main axis during the spin transition. As explained in ref. [23], despite the overall volume expansion, the films of **(1)** are expected to shrink in the *001* crystal planes parallel to the substrate surface. By assuming that the *a*- and *b*-axis would be randomly oriented in this plane an axial strain of $\frac{\epsilon_a+\epsilon_b}{2} = -0.65\ \%$ is expected to build up when going from the LS to the HS phase. The reduced value of the experimentally observed strain with respect to this theoretical value is not unusual for polycrystalline films.[55] On one hand the measured strain encompasses different effects arising from the microstructure of the films (in-plane texture, defects, grain boundary effects, internal stresses, etc.). More fundamentally, the strain is partially restricted by the substrate, which is precisely the origin of the generated stress causing it to bend.

From the strain, the work density W/V as well as the reactive force F associated with the SCO can be calculated from:

$$W/V = \frac{1}{2}Y_{SCO}\epsilon_{SCO} \quad (13)$$

and

$$F = \frac{3\epsilon_{SCO}}{2l}\frac{wt^2Y_{SCO}}{2}\frac{m}{(1+m)(1+mn)} \quad (14)$$

The work density is $\frac{W}{V} = 15 \pm ?\ mJ.cm^{-3}$, the reactive force at the end of the cantilever is $|F| = 1.02 \pm 0.02\ \mu N$ and its normalized value $|F_{norm}| = \frac{FL}{wt^2} = 883 \pm 25\ kPa$. Finally, using the equation of Stoney[56], the recoverable stress produced by the SCO strain is estimated as:

$$\sigma_{res} = \frac{1}{6} E_{Si} \frac{t_{Si}^2}{t_{SCO}} \kappa = -21 \pm 1\ MPa \quad (15)$$

Despite the particularly unfavorable growth direction of the films on the substrate - the highest strain *c*-axis being perpendicular to the cantilever axis – the evaluated stress and work density are very relevant for actuating purposes.[57]

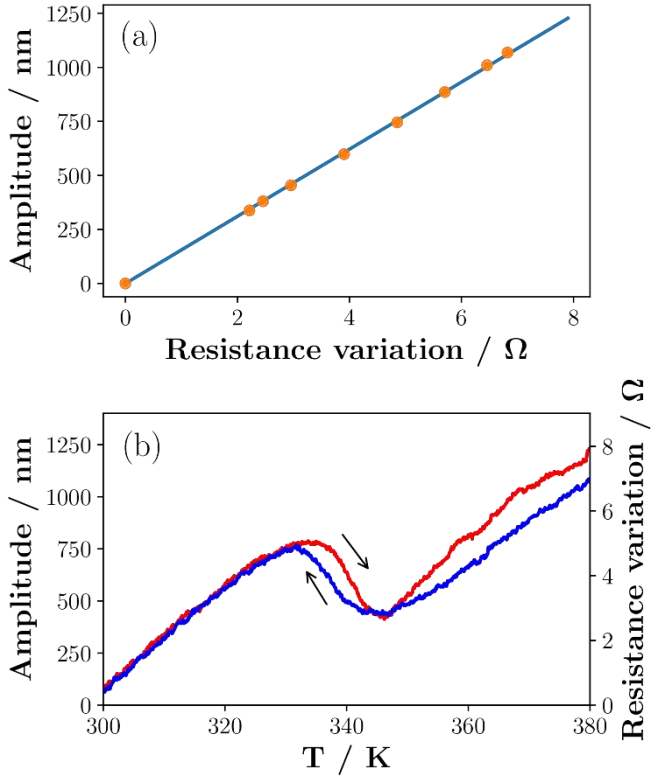

Figure 9. (a) Deflection amplitude *vs.* piezoresistance variation calibration curve for MEMS cantilevers. (b) Temperature dependence of the deflection amplitude of a MEMS cantilever (200×50×2 µm^3) actuated by a 140 nm thick film of **(1)**. Increasing amplitude corresponds to the upward deflection of the cantilever. Arrows indicate heating and cooling. (The piezoresistance values were published in ref. [23].)

4. Conclusions

In summary, by combining nuclear inelastic scattering, high pressure single-crystal X-ray diffraction and micromechanical resonance experiments on cantilevers, we have achieved a complete characterization of the elastic properties of the molecular SCO compound [Fe(HB(tz)$_3$)$_2$]. Through these different experimental techniques, we were able to extract a

unique combination of elastic constants including the effective bulk modulus, the Poisson's ratio, the Debye sound velocity and the Young's modulus. These measurements reveal a relatively large stiffness with a pronounced anisotropic change of the elastic moduli upon the spin transition. These different characteristics must be correlated with the strong cooperativity (of elastic origin) observed in this compound that manifests itself by an extremely abrupt, fast and robust spin transition. The knowledge of elastic properties allowed also for the full assessment of actuating performance of thin films of $[Fe(HB(tz)_3)_2]$. While these values are indeed relevant for actuating purposes there is a clear scope for future improvement by developing film growth methods, which allow to change to crystallographic orientation of the films with respect to the substrate.

5. Experimental Section

Synthesis: The synthesis of the powder and single crystal samples is described in Ref. [27].

Nuclear Inelastic Scattering: NIS measurements were performed at the Nuclear Resonance beamline ID18 of the European Synchrotron Radiation Facility (ESRF, Grenoble) in 16-bunch mode at 295 and 360 K using a home-made furnace and a fully ^{57}Fe-enriched powder of **(1)**. Details of the NIS setup and data acquisition are described in Ref. [33].

X-ray diffraction under high pressure: The synchrotron powder XRD experiments were carried out at the high pressure diffraction beamline ID15b of the European Synchrotron Radiation Facility (ESRF, Grenoble). The single crystal sample was compressed in a diamond anvil cell and the pressure was measured using the ruby fluorescence technique. The pressure transmitting medium was Daphne oil and the used beam wavelength was 30 keV. More details and refs?

Micromechanical measurements: Standard microfabrication process of bridges and cantilevers was done as described in ref. [18]. A SOI wafer (2 μm Si, 1 μm SiO_2, 400 μm thick Si) from Soitec was used and the microstructures were patterned using UV-photolithography (ECI 3012 photoresist), followed by a vertical RIE (reactive ion etching) and wet HF etching. At the final step, 210 nm thickness of **(1)** was deposited using the two-step procedure described in ref. [29], which consists of the thermal evaporation of **(1)** at 423 K under high vacuum (2×10^{-7} mbar) at a rate of 0.03 $A^{\circ}s^{-1}$ followed by a subsequent solvent vapor annealing. The device geometry and film quality were controlled by scanning electron microscopy using a Hitachi S-400 instrument and atomic force microscopy using a Cypher- ES system (Oxford Instruments) in tapping mode. Film thickness was controlled by a mechanical profilometer. In order to produce the mechanical movement, the sample is mounted on a motorized stage, placed inside a vacuum chamber (10^{-1} mbar). A piezo-shaker actuates in a collective manner all the devices on the chip

and their movement is detected one-by-one using optical interferometry.[38] To this aim, a He-Ne laser beam (λ = 632 nm, 30 mW rated power) is expander (×5) and focused by a microscope objective (× 20, N.A. 0.28) on the selected surface area of the sample. The air gap between the resonator (bridge or cantilever) and the substrate surface provides a Fabry-Perot cavity. The beam is deflected towards a photo-detector (New Focus 1601) from which the AC signal is connected to a Network Analyzer (Agilent 4395A) to track the response of the micromechanical structure at the excitation frequency.

Supporting Information

Supporting Information is available from the Wiley Online Library or from the author.

Acknowledgements

This work was supported by the Federal University of Toulouse through the project IDEX Emergence NEMSCOOP (ANR-11-IDEX-0002-02), the Région Occitanie (No. 15050450) and the French RENATECH network. The Ph.D. Grants of S.R., A.C.B. and M.D.M.J. were financed, respectively, by the French Ministry of Research, the Région Occitanie (No. 15050123) and the CONACYT (No. 382038).

Received: ((will be filled in by the editorial staff))
Revised: ((will be filled in by the editorial staff))
Published online: ((will be filled in by the editorial staff))

References

[1] P. Gütlich, A. Hauser, H. Spiering, *Angew. Chem., Int. Ed.* **199**4, *33*, 2024.
[2] P. Gütlich, H. A. Goodwin, *Top. Curr. Chem.* **2004**, Vols. *233*, *234*, *235*.
[3] M. A. Halcrow, Ed. , *Spin-Crossover Materials: Properties and Applications*, John Wiley & Sons Ltd, Oxford, UK, **2013**.
[4] G. Molnár, S. Rat, L. Salmon, W. Nicolazzi, A. Bousseksou, *Adv. Mater.* **2018**, *30*, 17003862.
[5] P. Guionneau, *Dalton. Trans.* **2014**, *43*, 382.
[6] H. Spiering, E. Meissner, H. Koppen, E. W. Muller, P. Gutlich, *Chem. Phys.* **1982**, *68*, 65.
[7] N. Willenbacher, H. Spiering, *J. Phys. C* **1988**, *21*, 1423.
[8] H. Spiering, K. Boukheddaden, J. Linares, F. Varret, *Phys. Rev. B* **2004**, *70*, 184106.
[9] J. Jung, F. Bruchhäuser, R. Feile, H. Spiering, P. Gütlich, *Z. Für Phys. B Condens. Matter* **1996**, *100*, 517.
[10] T. Granier, B. Gallois, J. Gaultier, J. A. Real, J. Zarembowitch, *Inorg. Chem.* **1993**, *32*, 5305.
[11] H.J. Shepherd, T. Palamarciuc, P. Rosa, P. Guionneau, G. Molnár, J.-F. Létard, A. Bousseksou, *Angew. Chem. Int. Ed.* **2012**, *51*, 3910.
[12] H. J. Shepherd, P. Rosa, L. Vendier, N. Casati, J.-F. Létard, A. Bousseksou, P. Guionneau, G. Molnár, *Phys. Chem. Chem. Phys.* **2012**, *14*, 5265.

[13] A. Tissot, H. J. Shepherd, L. Toupet, E. Collet, J. Sainton, G. Molnár, P. Guionneau, M.-L. Boillot, *Eur. J. Inorg. Chem.* **2013**, 1001.
[14] E. M. Hernández, C. M. Quintero, O. Kraieva, C. Thibault, C. Bergaud, L. Salmon, G. Molnár, A. Bousseksou, *Adv. Mater.* **2014**, *26*, 2889.
[15] G. Félix, M. Mikolasek, H. Peng, W. Nicolazzi, G. Molnár, A. I. Chumakov, L. Salmon, A. Bousseksou, *Phys. Rev. B* **2015**, *91*, 024422.
[16] S. Rat, M. Mikolasek, J. S. Costá, A. I. Chumakov, W. Nicolazzi, G. Molnár, L. Salmon, A. Bousseksou, *Chem. Phys. Lett.* **2016**, *653*, 131.
[17] M. Mikolasek, G. Félix, H. Peng, S. Rat, F. Terki, A. I. Chumakov, L. Salmon, G. Molnár, W. Nicolazzi, A. Bousseksou, *Phys. Rev. B* **2017**, *96*, 035426.
[18] M. D. Manrique-Juarez, S. Rat, L. Mazenq, F. Mathieu, I. Séguy, T. Leïchlé, L. Nicu, L. Salmon, G. Molnár, A. Bousseksou, in *2017 19th Int. Conf. Solid-State Sens. Actuators Microsyst. TRANSDUCERS*, **2017**, pp. 1300–1303.
[19] H. J. Shepherd, I. A. Gural'skiy, C. M. Quintero, S. Tricard, L. Salmon, G. Molnar, A. Bousseksou, *Nat. Commun.* **2013**, *4*, 3607.
[20] I. A. Gural'skiy, C. M. Quintero, J. S. Costa, P. Demont, G. Molnar, L. Salmon, H. J. Shepherd, A. Bousseksou, *J. Mater. Chem. C* **2014**, *2*, 2949.
[21] Y.-C. Chen, Y. Meng, Z.-P. Ni, M.-L. Tong, *J. Mater. Chem. C* **2015**, *3*, 945.
[22] M. D. Manrique-Juarez, S. Rat, F. Mathieu, D. Saya, I. Séguy, T. Leichlé, L. Nicu, L. Salmon, G. Molnar, A. Bousseksou, *Appl. Phys. Lett.* **2016**, *109*, 061903.
[23] M. D. Manrique-Juárez, F. Mathieu, V. Shalabaeva, J. Cacheux, S. Rat, L. Nicu, T. Leïchlé, L. Salmon, G. Molnár, A. Bousseksou, *Angew. Chem. Int. Ed.* **2017**, *129*, 8186.
[24] M. Urdampilleta, C. Ayela, P.-H. Ducrot, D. Rosario-Amorin, A. Mondal, M. Rouzieres, P. Dechambenoit, C. Mathoniere, F. Mathieu, I. Dufour, R. Clerac, arXiv:1701.01341.
[25] M. D. Manrique-Juárez, F. Mathieu, A. Laborde, S. Rat, V. Shalabaeva, P. Demont, O. Thomas, L. Salmon, T. Leichle, L. Nicu, G. Molnár, A. Bousseksou, *Adv. Funct. Mater.* **2018**, in press.
[26] S. Trofimenko, *J. Am. Chem. Soc.* **1967**, *89*, 3170.
[27] S. Rat, K. Ridier, L. Vendier, G. Molnár, L. Salmon, A. Bousseksou, *CrystEngComm* **2017**, *19*, 3271.
[28] K. Ridier, S. Rat, L. Salmon, W. Nicolazzi, G. Molnár, A. Bousseksou, P*hys. Chem. Chem. Phys*. **2018**, in press, DOI: 10.1039/C7CP08522B.
[29] V. Shalabaeva, S. Rat, M. D. Manrique-Juarez, A.-C. Bas, L. Vendier, L. Salmon, G. Molnár, A. Bousseksou, *J. Mater. Chem. C* **2017**, *5*, 4419.
[30] V. Shalabaeva, M. Mikolasek, M. D. Manrique-Juarez, A.-C. Bas, S. Rat, L. Salmon, W. Nicolazzi, G. Molnár, A. Bousseksou, *J. Phys. Chem. C* **2017**, *121*, 25617.
[31] M. D. Manrique-Juarez, F. Mathieu, V. Shalabaeva, J. Cacheux, S. Rat, L. Nicu, T. Leïchlé, L. Salmon, G. Molnár, A. Bousseksou, *Angew. Chem.* **2017**, *129*, 8186.
[32] R. Rüffer, A. I. Chumakov, *Hyperfine Interact.* **1996**, *97–98*, 589.
[33] A. I. Chumakov, W. Sturhahn, *Hyperfine Interact.* **1999**, *123–124*, 781.
[34] M. Y. Hu, W. Sturhahn, T. S. Toellner, P. D. Mannheim, D. E. Brown, J. Zhao, E. E. Alp, *Phys. Rev. B* **2003**, *67*, 094304.
[35] K. Achterhold, C. Keppler, A. Ostermann, U. van Bürck, W. Sturhahn, E. E. Alp, F. G. Parak, *Phys. Rev. E* **2002**, *65*, 051916.
[36] L. M. Thomas, J. Shanker, *Phys. Status Solidi B* **1995**, *189*, 363.
[37] J. A. Hoy-Benítez, F. Avilés, F. Gamboa, R. Peón-Escalante, A. I. Oliva, *Meas. Sci. Technol.* **2012**, *23*, 045605.
[38] A. Bhaswara, D. Dezest, L. Nicu, T. Leichle, B. Legrand, in *Solid-State Sens. Actuators Microsyst. TRANSDUCERS 2015 Transducers-2015 18th Int. Conf. On*, IEEE, **2015**, pp. 2200–2203.

[39] M. A. Hopcroft, W. D. Nix, T. W. Kenny, *J. Microelectromechanical Syst.* **2010**, *19*, 229.
[40] J. Laisney, H. J. Shepherd, L. Rechignat, G. Molnár, E. Rivière, M.-L. Boillot, submitted.
[41] T. Romero-Morcillo, M. Seredyuk, M. C. Munoz, J. A. Real, *Angew. Chem. Int. Ed.* **2015**, *54*, 14777.
[42] O. Roubeau, J. M. Alcazar Gomez, E. Balskus, J. J. A. Kolnaar, J. G. Haasnoot, J. Reedijk, *New J. Chem.* **2001**, *25*, 144.
[43] G. Félix, M. Mikolasek, H. Shepherd, Y. Guari, A. Chumakov, J.-P. Itié, W. Nicolazzi, G. Molnár, A. Bousseksou, *Eur. J. Inorg. Chem.* **2018**, 443.
[44] J. J. McKinnon, D. Jayatilaka, M. A. Spackman, *Chem. Commun.* **2007**, 3814.
[45] J. J. McKinnon, M. A. Spackman, A. S. Mitchell, *Acta Crystallogr.* **2004**, *B60*, 627.
[46] P. A. Wood, J. J. McKinnon, S. Parsons, E. Pidcock and M. A. Spackman, *CrystEngComm* **2008**, *10*, 368.
[47] J. Linares, H. Spiering, F. Varret, *Eur. Phys. J.* **1999**, *10*, 271.
[48] J-A. Real, H. Bolvin, A. Bousseksou, A. Dworkin, O. Kahn, F. Varret, J. Zarembowitch, *J. Am. Chem. Soc.* **1992**, *114*, 4650.
[49] M. A. Halcrow, *Chem. Soc. Rev.* **2011**, *40*, 4119.
[50] G. Bradley, V. McKee, S. M. Nelson, *J. Chem. Soc. Dalton Trans.* **1978**, 522.
[51] J.-A. Real, B. Gallois, T. Granier, F. Suez-Panama, J. Zarembowitch, *Inorg. Chem.* **1992**, *31*, 4972.
[52] V. Niel, J. M. Martinez-Agudo, M. C. Munoz, A. B. Gaspar, J. A. Real, *Inorg. Chem.* **2001**, *40*, 3838.
[53] P. D. Southon, L. Liu, E. A. Fellows, D. J. Price, G. J. Halder, K. W. Chapman, B. Moubaraki, K. S. Murray, J.-F. Létard, C. J. Kepert, *J. Am. Chem. Soc.* **2009**, *131*, 10998.
[54] H. Spiering, *Top. Curr. Chem.* **2004**, *235*, 171.
[55] E. Merced, X. Tan, N. Sepulveda, *Sensors Actuators A* **2013**, *196*, 30.
[56] G. Stoney, *P. Roy. Soc. A. Math Phy.* **1909**, *82*, 172
[57] S. Mirvakili, I.W. Hunter, *Adv. Mater.* **2018**, *30*, 1704407.